Nano Research

Open Access

Research Article

Lamellar P-type molecular sieve modified separators for suppressing lithium dendrites in lithium metal battery

Fei Sha[1], Yingying Deng[1], Suyang Wang[1], Peng Wang[2]✉, Jinyan Hu[1], Kening Sun[1], Qi Sun[1]✉, and Jiao-Jing Shao[1]✉

[1] College of Materials and Metallurgy, Guizhou University, Guiyang 550025, China
[2] School of Chemical Engineering, Zhengzhou University, Zhengzhou 450001, China

Cite this article: *Nano Research*, **2026**, *19*, 94908517. https://doi.org/10.26599/NR.2026.94908517

ABSTRACT: Lithium metal batteries (LMBs) have undergone extensive development owing to their remarkable energy storage capabilities. Nevertheless, safety concerns, including thermal runaway and lithium dendrites, impede their application. Modification of separators can effectively overcome the limitations of commercial separators, such as inferior thermal stability and poor wettability, and consequently alleviate the damage induced by lithium dendrites. Here, we synthesize a three-dimensional P-type molecular sieve and develop a lamellar-structured material, which is then used to fabricate composite separators by coating it onto polypropylene (PP) separators (denoted as PP@3DP and PP@TOC/3DP). Experimental results demonstrate that, in comparison with pristine PP separators, the composite separators display significantly enhanced physical properties, such as improved porosity, thermal stability, and tensile strength. The battery assembled with the PP@TOC/3DP separator exhibits a higher initial discharge specific capacity (167.96 mAh·g^{-1}), superior rate performance, and enhanced cycling stability at 0.5 C, compared to batteries assembled with the PP separator and the PP@3DP separator. Moreover, after 1000 cycles at 2.0 C, it sustains a capacity retention rate of 95.90% with a specific capacity of 140.36 mAh·g^{-1}. These findings strongly attest to the excellent performance of PP@TOC/3DP and pave the way for molecular sieve functionalized separators in LMBs.

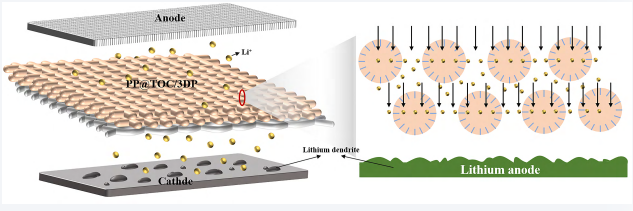

KEYWORDS: lithium metal battery, P-type molecular sieve, separator modification, lithium dendrite

1 Introduction

With the in-depth implementation of global energy transition and sustainable development strategies, lithium metal batteries (LMBs), utilizing lithium metal as the negative electrode, are acknowledged as the core development direction for next-generation high-energy-density battery systems owing to their extremely low redox potential and ultra-high theoretical specific capacity [1]. However, during the cycling process, the uneven deposition of lithium ions on the negative electrode surface induces the growth of lithium dendrites, which may lead to short-circuits, capacity fading, and a reduction in Coulombic efficiency [2]. Furthermore, a high chemical reactivity exists between lithium metal and the electrolyte, resulting in the formation of an inhomogeneous and mechanically weak solid electrolyte interphase (SEI) layer. This layer is prone to rupture, causing electrolyte consumption, loss of active lithium, exacerbating the growth of lithium dendrites, and ultimately triggering serious thermal-runaway safety accidents [3, 4]. As a core component of LMBs, the separator, typically made of polyethylene (PE) and polypropylene (PP), serves the crucial function of maintaining a physical separation between the positive and negative electrodes [5, 6]. This separation effectively prevents short-circuits that may arise from physical contact, while simultaneously facilitating the efficient transfer of lithium ions. Moreover, the surface modification of separators through coating with specific substances can notably enhance the cycle stability and safety of LMBs [7, 8]. For example, Ankush Singh et al. [9] prepared a zinc oxide-coated PP separator using an adhesive-free method, ultimately achieving stable lithium deposition by inducing the *in-situ* formation of a zinc-rich solid electrolyte interphase. Liu et al. [10] employed a PP separator modified with high-entropy oxide multi-shell hollow spheres, which exhibited excellent ionic conductivity and wettability and can accelerate lithium ion diffusion and homogenize the lithium ion flux.

Molecular sieves are a class of high-performance silicoaluminate

Received: October 18, 2025; **Revised:** January 9, 2026
Accepted: February 1, 2026

✉Address correspondence to Peng Wang, pengwang240824@zzu.edu.cn; Qi Sun, qsun@gzu.edu.cn; Jiao-Jing Shao, xjshao@gzu.edu.cn

porous materials. Their advantage lies in the special framework structure formed by the interconnection of SiO_4^- and AlO_4^- units [11]. This architecture endows the material with molecular-scale uniform and tunable pores, outstanding thermal and chemical stability, as well as abundant cation-exchange sites anchored at tetrahedra, thus conferring superior ionic conductivity [12]. Recently, numerous researchers have focused on this material, using it as a modifier for separators and verifying its substantial potential in LMBs. Yu et al. [13] designed a composite separator based on two-dimensional Mobil Five (MFI)-type zeolite nanosheets (or two-dimensional MFI-type zeolite nanosheets), which improved electrolyte wettability and enhanced lithium ion conductivity through size sieving, thereby suppressing the shuttle effect of lithium polysulfides. Wang et al. [14] proposed a design of a two-dimensional A-type zeolite-coated PP separator, which can promote uniform lithium ion transport and effectively suppress the formation of lithium dendrites. More remarkably, P-type molecular sieves, which feature a gismondine (GIS) structure with an eight-membered ring cross-channel, possess a large specific surface area, excellent thermal shrinkage properties, strong mechanical properties, and customizable surface and chemical characteristics, making them suitable for the modification of separators in LMBs [15]. Furthermore, due to their distinct features, such as a regular pore channel structure, high specific surface area, and adjustable ion exchange capacity, they exhibit unique advantages in battery technology, particularly in enhancing energy density, cycle life, and safety [16, 17].

In this study, two inorganic particle functional coatings (PP@3DP and PP@TOC/3DP) are constructed on PP separators by the coating method. The lamellar TOC/3DP enhances the specific surface area and pore structure, exposing more active sites. This not only facilitates the formation of a more uniform SEI layer and the regulation of homogeneous lithium deposition but also establishes rapid lithium-ion migration channels. The influence of lithium-ion transport and lithium dendrite growth in different separators is shown in Fig. 1(a). Research indicates that the PP@TOC/3DP separator exhibits high thermal stability, excellent electrolyte wettability, and porosity. The LMBs assembled with the PP@TOC/3DP separator initially deliver a discharge specific capacity of 167.96 mAh·g^{-1} at 0.5 C. After 300 cycles, the capacity retention rate is 97.23%. Meanwhile, after 800 cycles at 1.0 C and 1000 cycles at 2.0 C, the capacity retention rates are 94.92% and 95.90%, respectively, effectively prolonging the cycle life of the battery.

2 Experimental

2.1 Materials

Natural kaolin was provided by Guizhou New Materials Technology Co., Ltd., whose main chemical composition consists of silicon dioxide (SiO_2, 55.5 wt.%) and aluminum oxide (Al_2O_3, 39.2 wt.%). Sodium hydroxide (NaOH, 96%, analytical reagent (AR)) was purchased from Shanghai Maclean Biochemical Technology Co., Ltd. Cetyltrimethylammonium bromide (CTAB, 99%, AR), tetrabutylammonium hydroxide solution (TBAOH, AR), and N-methylpyrrolidone (NMP, 99.0%, gas chromatography (GC)) were all purchased from Shanghai Aladdin Biochemical Technology Co., Ltd. Cegard 2500 PP separator was used as the substrate. Polyvinylidene fluoride (PVDF, anhydrous), lithium electrolyte (diethyl carbonate (DEC):ethylene carbonate (EC):dimethyl carbonate (DMC) = 1 vol.%:1 vol.%:1 vol.%), $LiFePO_4$ (LFP), and acetylene black (ACET) were all purchased from Dongguan Keruide Experimental Equipment Technology Co., Ltd. Deionized water was prepared in the laboratory.

2.2 Preparation of composite separator

Taking P-type molecular sieve as an example: 3DP powder and PVDF were weighed with a mass ratio of 8:1; they were ground in a mortar for 30 min; then, 2.5 mL of NMP solvent was added using a pipette, ultrasonically dispersed for 15 min, and then magnetically stirred at room temperature for 8 h to obtain a uniform mixed slurry. The slurry was evenly applied onto the PP separator using a 50 μm scraper. Then, the coated separator was placed in a 50 °C forced-air drying oven and allowed to stand for 30 min. After that, it was transferred to a constant temperature oven for drying overnight. When in use, the separator was cut into round plates with a diameter of 16 mm using a tablet press for later use.

2.3 Material characterization

The crystal structure and image analysis calculation were analyzed by X-ray diffraction (XRD, Panalytical Empyrean, Netherlands) characterization of the samples using Cu-Kα-rays (45 kV, 40 mA, λ = 0.15406 nm, 10 °·min^{-1}, room temperature). The molecular structure and groups of the material were determined by using a Fourier transform infrared (FTIR) spectrometer (Thermo Scientific Nicolet 6700, USA). The specific surface area and pore size distribution of the material were determined by using the fully automatic specific surface area and pore size analyzer (Brunauer–Emmett–Teller (BET), Micromeritics ASAP 2460, USA) for analysis. The microscopic morphology, electron diffraction, and elemental distribution of the samples were observed by transmission electron microscope (TEM, FEI Tecnai G2 F20 S-TWIN, USA) and field emission scanning electron microscope (SEM, Zeiss Sigma 300, Germany). The affinity of the composite separator for the electrolyte was detected using a contact Angle meter (JC2000D1, Zhongchen, Shanghai, China).

2.4 Assembly and testing of batteries

The CR2032 button battery assembled in this study had $LiFePO_4$ as the positive electrode active material. It was mixed with an appropriate amount of solvent NMP in a ratio of active material:conductive agent:binder = 8:1:1 and ground into a uniform electrode material. Then, it was applied to the carbon-coated aluminum foil using a 75 μm scraper. The coated electrode sheet was vacuum-dried at 90 °C for 12 h. Then it was cut into round pieces with a diameter of 12 mm and set aside. The negative electrode adopted lithium metal sheets, the electrolyte was 1 mol $LiPF_6$, EC + DEC + DMC (1 vol.%:1 vol.%:1 vol.%), and the separator was a PP separator and a laboratory-made composite separator.

The entire battery assembly process was carried out in a glove box filled with argon gas, and the water and oxygen content generally had to be below 0.1 ppm. The assembly sequence was as follows (taking the assembly of PP separators as an example): First, a lithium metal sheet was placed in the negative electrode shell, followed by the addition of 25 μL of electrolyte. Subsequently, the separator was mounted (with the slurry-coated side of the composite separator facing the positive electrode for assembly), and the same volume of electrolyte was added again. Subsequently, the positive electrode sheet, stainless steel gasket, spring, and positive electrode shell were placed in sequence, and the assembly was sealed with a sealing machine to obtain the button battery. The

assembled battery was left to stand for 12 h to allow the electrolyte to fully wet the separator. Subsequently, rate cycling and long cycling tests were conducted on the NEWARE CT-4008T testing system, and tests, such as linear scanning voltammetry (LSV), cyclic voltammetry (CV), and alternating current (AC) impedance (0.01–100 kHz), were carried out on the CS studio5 electrochemical workstation.

3 Results and discussion

3.1 Morphology and structural characterization

The XRD patterns of as-synthesized P-type zeolite and layered TOC/3DP are shown in Fig. S1 in the Electronic Supplementary Material (ESM). Both exhibit characteristic peaks of P-type zeolite consistent with the standard JCPDS card (No. 44-0052). The 2θ values correspond to the crystal faces as follows: 12.44° for (101), 17.68° for (200), 21.65° for (112), 25.27° for (220), 28.16° for (301), 33.32° for (312), 35.65° for (004), 38.34° for (411), 44.39° for (422), 46.07° for (314), and 49.88° for (512). The XRD patterns show that the impurity peaks can be ignored. It has excellent crystallinity and sample purity, and all exhibit the characteristic diffraction peaks of GIS zeolite, belonging to the P (Na) structure of zeolite. FTIR spectroscopy shows that TOC/3DP presents the skeleton structure of 3DP molecular sieves. The peak at 438.769 cm^{-1} is the bending vibration peak of NaP molecular sieve Si–O, confirming the silicoaluminate skeleton structure of the molecular sieve. The peak at 612.923 cm^{-1} is the double-ring vibration absorption peak externally connected to the NaP molecular sieve. Here, it indicates that the crystal frameworks of the two materials are double-ring structures. The peaks at 679.762 and 742.923 cm^{-1} are the symmetrical stretching vibration absorption peaks and asymmetric stretching vibration absorption peaks of the Si–O tetrahedron of NaP molecular sieve, mainly caused by the valence vibration of the (Al, Si)–O bond, further indicating that both synthesized samples have the framework structure of molecular sieve. The peak at 990.692 cm^{-1} is the asymmetric stretching vibration peak of SiO_4^- and AlO_4^- tetrahedra inside the NaP molecular sieve. Among them, the asymmetric stretching vibration peak of Si–O–Si is one of the characteristic peaks of the molecular sieve skeleton structure, with a relatively high intensity, indicating the presence of silicon–oxygen tetrahedra in the structures of the two synthesized samples. The TOC/3DP coating has an absorption peak at 1435.434 cm^{-1} in the spectrum, which is mainly caused by the bending vibration of the C–H bond in the template agent TBAOH. The 1641.007 cm^{-1} absorption peak is caused by the bending vibration of –OH adsorbed water and is another absorption peak of water molecules existing in the pore structure of molecular sieves. A relatively wide absorption peak appears at 3437.076 cm^{-1}, which is the stretching vibration peak of the –OH groups on the surface of the molecular sieve adsorbing water. Due to the hydrogen bonds between water molecules, the absorption peak is relatively wide in Fig. S2 in the ESM. The XRD and FTIR patterns indicate that the TOC/3DP synthesized with TBAOH as a template agent has a framework structure that is basically consistent with that of the three-dimensional P-type zeolite. The introduction of the template agent does not alter the original framework structure of the zeolite, but only affects its morphological characteristics. This further verifies that the template agent primarily functions to regulate the morphology in this synthesis system without interfering with the inherent structural properties of the framework.

To evaluate the adsorption performance and pore structure characteristics of 3DP and TOC/3DP, adsorption–desorption experiments are conducted on the two samples under a N_2 atmosphere. The results are analyzed using the BET equation and International Union of Pure and Applied Chemistry (IUPAC) classification standards. According to the IUPAC classification, the isotherms of P-type molecular sieves all belong to Type-IV, while TOC/3DP also exhibits typical H4-type hysteretic loops, indicating that mesoporous structures exist in all samples [18]. Since both have slit pores formed by grain accumulation in their pore structures, the desorption process is affected by the "bottleneck effect", and hysteresis loops appear on the isotherms, which is consistent with the characteristics of typical microporous materials [19, 20]. From the perspective of adsorption behavior, in the low relative pressure range (P/P_0 = 0–0.5), the adsorption capacity of N_2 does not increase significantly, but the adsorption capacity of TOC/3DP is significantly greater than that of 3DP. When P/P_0 reaches 0.8, the adsorption capacity rises sharply, and eventually, the N_2 adsorption capacity of TOC/3DP is approximately 1.5 times that of 3DP. The BET equation calculation results show that the total specific surface area (365.689 $m^2 \cdot g^{-1}$), micropore specific surface area, and micropore volume of TOC/3DP are much higher than those of 3DP (the total specific surface area is only 12.803 $m^2 \cdot g^{-1}$) [21, 22]. The reason is that the lamellar structure of TOC/3DP can expose more porous structures, and the interlamellar gaps provide new pores. Barrett–Joyner–Halenda (BJH) equation analysis indicates that the main pore size distribution ranges of 3DP and TOC/3DP are 2–140 nm, suggesting that the template agents (TBAOH) do not alter the overall pore size range of the P-type molecular sieve. However, due to the tetrahedral structure as the unit, 3DP forms straight or sinusoidal channels through stacking [23], resulting in a wider pore size distribution. In contrast, the voids formed by the superposition of TOC/3DP sheets are smaller, and the pore size distribution is narrower, with the main pore size range concentrated within 1.5 to 15 nm in Fig. S3 and Table S1 in the ESM. Among the critical indicators determining the performance of molecular sieves are specific surface area and pore diameter. TOC/3DP exhibits superior pore structure parameters (larger specific surface area, greater number of micropores, and larger micropore volume), resulting in significantly better performance compared to traditional three-dimensional P-type molecular sieves.

To systematically evaluate the thermal behavior characteristics of TOC/3DP samples, experiments are conducted using a synchronous thermal analyzer for thermogravimetric-differential scanning calorimetry (TG-DSC) analysis under an inert argon atmosphere. This instrument can accurately characterize key parameters of the samples, such as thermal stability and phase transition temperatures. The weight loss behavior and reaction characteristics of the sample across different temperature ranges can be clearly observed from the TG–derivative thermogravimetry (DTG) curves (Fig. S4 in the ESM). In the temperature range of 400–470 K, the sample shows a significant weight loss phenomenon, with a weight loss rate as high as 9.00%. Meanwhile, the DTG curve presents a distinct absorption peak at 370 K. This process corresponds to the extensive removal of surface adsorbed water in the TOC/3DP laminate structure. As the temperature further increases to 550–650 K, the sample enters the second stage of weight loss, with a weight loss rate of 3.31% in this interval. This is mainly attributed to the desorption of chemically adsorbed water

in the TOC/3DP pores and the decomposition reaction of Al–OH groups in the aluminum oxide tetrahedra [24, 25]. When the temperature continuously rises above 1000 K, the basic framework structure of TOC/3DP begins to gradually collapse and eventually undergoes decomposition and damage [26]. At this stage, the weight loss rate is only 0.96%. Based on the thermal behavior analysis of multiple temperature ranges mentioned above, it can be concluded that TOC/3DP can maintain structural stability below 1000 K, with only moisture removal and group decomposition occurring, and destruction does not occur until above 1000 K, which fully demonstrates its excellent thermal stability.

The morphology of PP@TOC/3DP is analyzed by TEM. The sample has a thin sheet structure, which is semi-transparent, confirming the morphology of the PP@TOC/3DP lamellar structure in Fig. 1(b). The analysis in Fig. 1(c) indicates the characteristics of the TO_4^- (T is Si or Al) tetrahedral structure. This further confirms that TOC/3DP possesses the structural characteristics of 3DP molecular sieves, which is consistent with the results of XRD studies. Clear lattice fringes are shown in Fig. 1(d), characterized by a crystal plane spacing of 0.337 nm, corresponding to the (220) crystal plane. Meanwhile, the thickness of the layered coating is measured to be 0.371 nm in Fig. 1(e). Furthermore, the

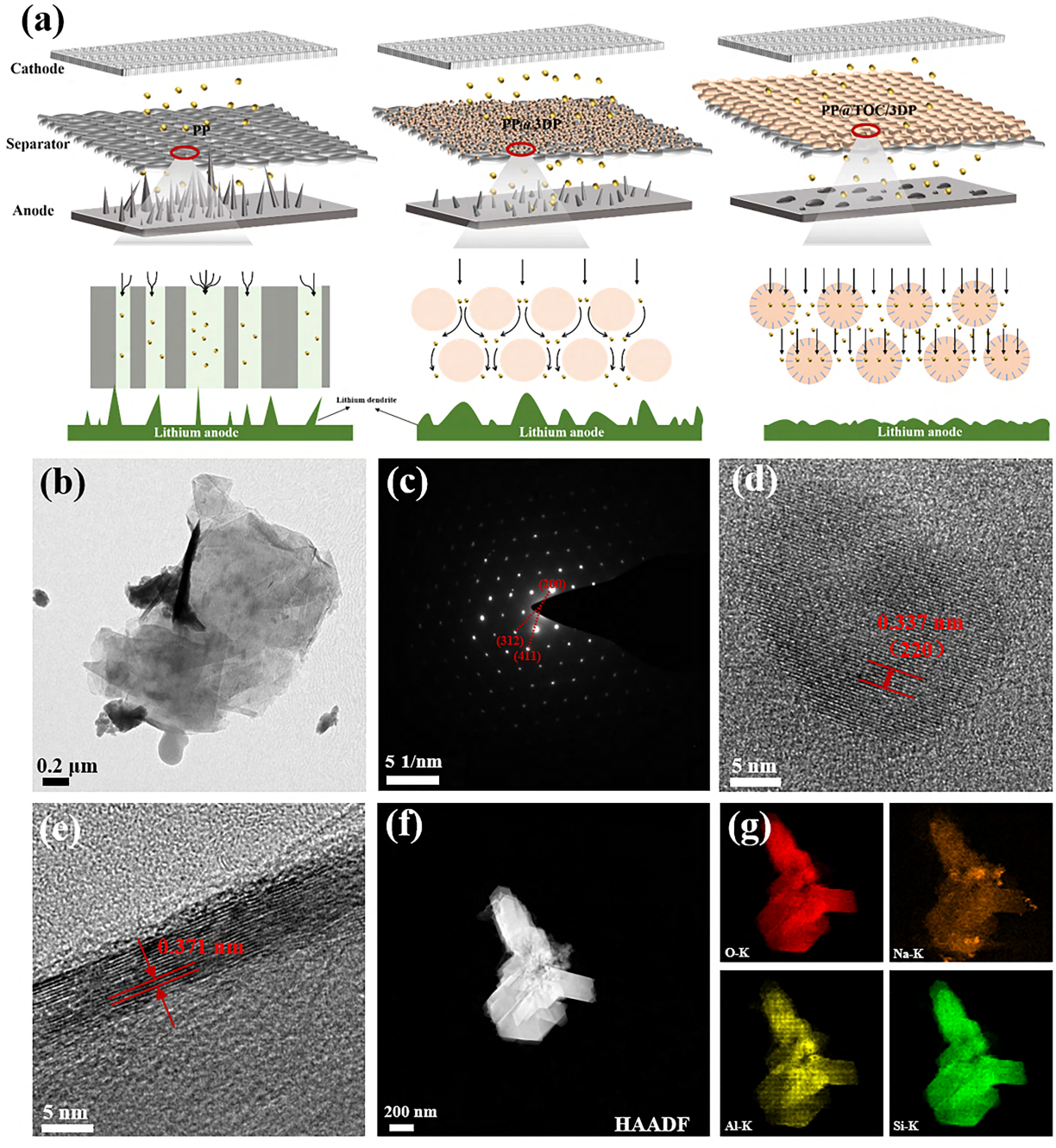

Figure 1 (a) Schematic illustration of PP separators modified with different coatings. (b) TEM image of the TOC/3DP molecular sieve. (c) Selected-area electron diffraction (SAED) pattern of TOC/3DP. (d) High-resolution TEM (HRTEM) image showing lattice fringes of TOC/3DP. (e) HRTEM image indicating the thickness of the molecular sieve. (f) High-angle annular dark-field scanning TEM (HAADF-STEM) image of TOC/3DP. (g) Elemental mapping images of O, Na, Al, and Si in TOC/3DP.

element mapping further confirms that the Si, Al, Na, and O elements are uniformly distributed on the surface of the laminate TOC/3DP (Figs. 1(f) and 1(g)).

3.2 Characterization of separator

The SEM images show completely different surface morphologies of the separator. The commercial separator Cegard 2500 is produced by a unidirectional stretching process [27]. The micropores of the PP separators are similar to an elliptical structure in Fig. 2(a). Since it is only stretched in one direction, the strength of the separator in the transverse direction is relatively poor, and its thickness is generally 25 μm [28, 29]. Figures 2(b) and 2(e) and Figs. 2(c) and 2(f) show the SEM images of the surface and cross-section of the PP@3DP and PP@TOC/3DP composite separator, respectively. Meanwhile, the state of the PP@TOC/3DP coated PP separator is shown in Fig. 2(d), and it can be found in Fig. S5 in the ESM that the molecular sieve powder is successfully loaded onto the PP separator. The thickness of the PP@3DP coating is approximately 33.09 μm, and the thickness of the PP@TOC/3DP coating is approximately 32.13 μm. It can also be seen from the side that there are many pores in the stacking structure, which can increase the capacity of the composite separator to store electrolyte [30], which is conducive to the formation of flat-topped protrusions rather than sharp dendrites in the lithium stacking, effectively regulating lithium-ion flux and homogenizing lithium-ions [31].

3.3 Physical performance analysis of composite separator

The excellent mechanical properties of the separator can effectively block the piercing of lithium dendrites during their growth process, thereby significantly improving the safety coefficient of lithium batteries. The porosity of both PP@3DP and PP@TOC/3DP composite separators is substantially higher than that of the original PP separator in Fig. 3(a). This is because the modified separators are coated with a layer of porous inorganic particles, which introduce a large number of additional pore structures into the separator, directly contributing to the increase in porosity [32]. The thermal shrinkage rates of the PP@3DP and PP@TOC/3DP composite separators are 19.78% and 18.36%, respectively, while that of the original PP separator is as high as 41.23% in Fig. 3(b), indicating a significant gap among the three. This reason is that the inorganic particle coating applied has excellent thermal stability, effectively enhancing the dimensional stability of the original PP separator and thereby reducing the thermal shrinkage rate [33]. In addition, Fig. S6 in the ESM intuitively demonstrates the excellent thermal stability of the composite separator, a property that significantly enhances its application reliability and performance in high-temperature environments. Meanwhile, Fig. 3(c) shows that within each test period, the electrolyte absorption rate of the modified separator is higher than that of the PP separator, and the electrolyte holding rate has also been significantly improved. This reason is that the coating material itself has a rich pore structure, which can fully adsorb and retain the electrolyte, providing a guarantee for battery performance. In addition, the separator needs to have a certain mechanical strength to maintain structural integrity [34]. Therefore, tensile tests are conducted on PP, PP@3DP, and PP@TOC/3DP composite separators to compare their mechanical properties. The experimental results show that the tensile strength of the original PP separator is 74.20 MPa. After modification with the coating material, the tensile strengths of the PP@3DP and PP@TOC/3DP composite separators are increased to 103.43 and 99.44 MPa, respectively. From the tensile stress–strain curve, it can be seen that the plastic deformation zones of both composite separators are longer than those of the PP separator. In terms of elongation at break, PP@3DP is 38.54% and PP@TOC/3DP is 54.52%, with a difference of 15.98% between the two in Fig. 3(d). This series of data indicates that 3DP and TOC/3DP as coatings can significantly enhance the tensile strength of the separator. Among them, the modification effect of PP@TOC/3DP is more prominent, and both composite separators retain the original elastic and plastic properties of the PP separator. While performance is improved, the composite separator still maintains excellent flexibility. After folding tests, no powder shedding occurs on the coated surface, which remains uniform, intact, and tightly bonded to the base membrane (Fig. S7 in the ESM).

Additionally, the separator should possess excellent electrolyte

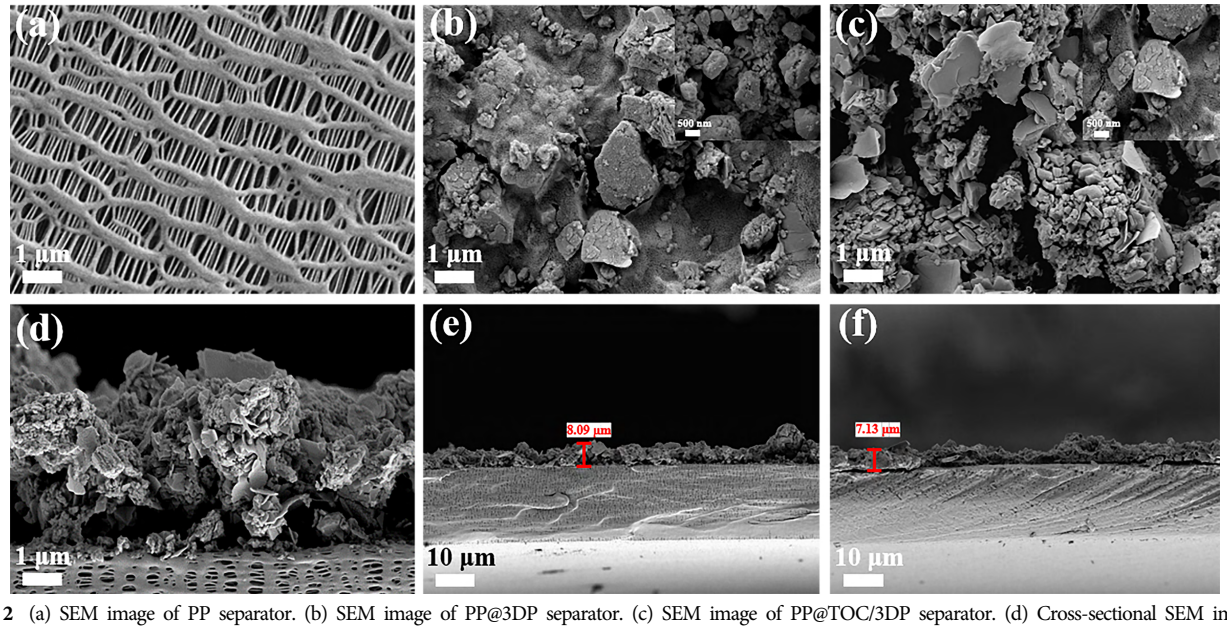

Figure 2 (a) SEM image of PP separator. (b) SEM image of PP@3DP separator. (c) SEM image of PP@TOC/3DP separator. (d) Cross-sectional SEM image of PP@TOC/3DP separator. ((e) and (f)) Cross-sectional thickness of PP@3DP and PP@TOC/3DP separators.

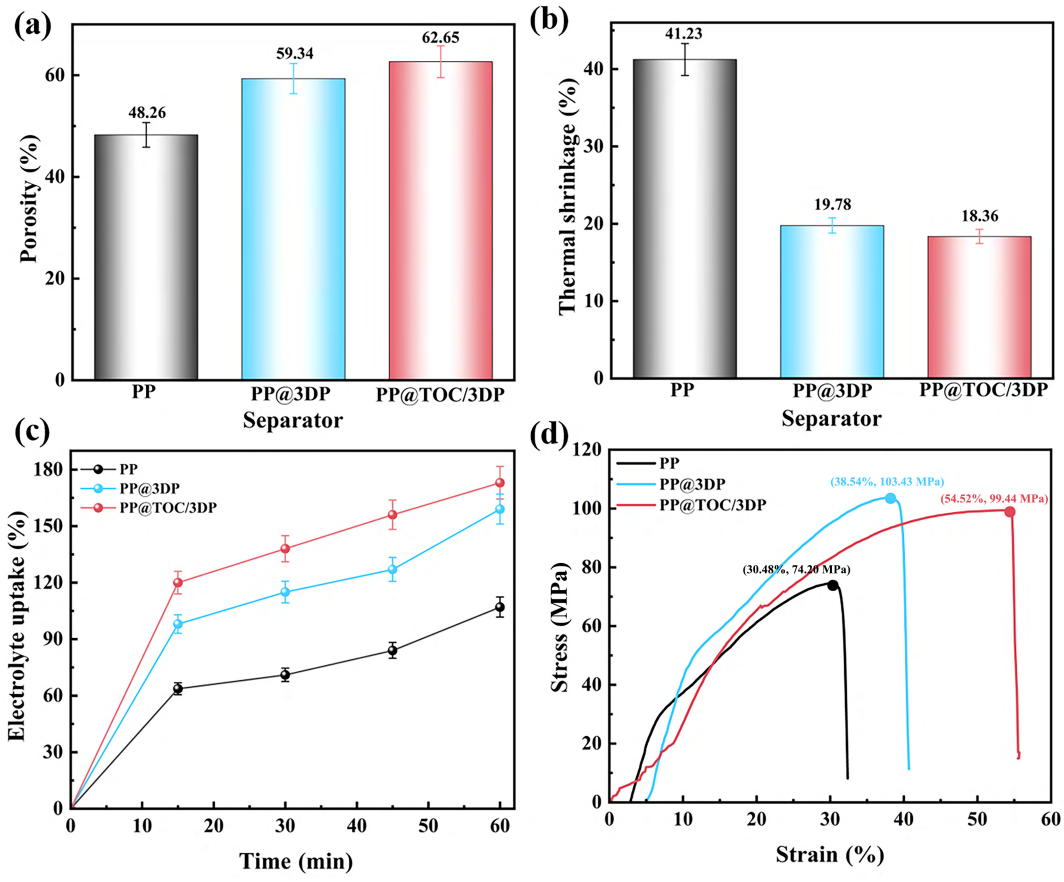

Figure 3 (a) Porosity, (b) thermal shrinkage rate, (c) electrolyte retention rate, and (d) tensile strength of PP, PP@3DP, and PP@TOC/3DP separators.

affinity to provide high electrolyte absorption and ionic conductivity. The wettability of different separators towards the electrolyte is compared. The electrolytes are dropped onto the surfaces of PP and PP@3DP, PP@TOC/3DP separators, respectively. The images of the electrolytes remaining stagnant on the separators for 8 s are recorded in Fig. S8 in the ESM. The results show that the changes of the electrolytes on the PP separators are slightly smaller, while PP@3DP and PP@TOC/3DP can quickly infiltrate. This is mainly because both the PP@3DP and PP@TOC/3DP surfaces are rich in –OH, which can form hydrogen bond networks with the electrolyte solvent, thereby increasing the affinity between the separator and the electrolyte [35, 36]. Meanwhile, the PP separator has an uneven water permeation problem, with local bulging and protrusion phenomena, indicating poor wetting permeability. However, the PP@3DP separator exhibits a regular circular distribution of water permeation areas, with the disappearance of bulging and protrusion, and a significant improvement in permeation uniformity. Moreover, the PP@TOC/3DP separator shows deeper water permeation coloring, a more uniform distribution, and further enhanced adsorption and permeation capacity (Fig. S9 in the ESM).

3.4 Electrochemical and cycling performance of the battery

From the LSV curves in Fig. 4(a), it can be observed that no redox peaks occur in the voltage range of 2.5–4.5 V for the three types of batteries, and the current remains flat and stable before 4.5 V. This indicates that all batteries in this range have good electrochemical stability [33]. When the voltage exceeds 4.5 V, the current increases as the voltage rises. This phenomenon is primarily associated with the oxidation and decomposition of the electrolyte. These findings demonstrate that the composite separator can satisfy the fundamental requirement of not reacting with solvents within the working voltage range of 2.5 to 4.5 V, making it entirely suitable for practical application scenarios in lithium metal batteries [37]. The results of studying mass transfer resistance in electrochemical performance through AC impedance spectroscopy under open-circuit conditions are shown in Fig. 4(b). Compared to batteries using PP separators, batteries assembled with PP@3DP and PP@TOC/3DP composite separators exhibit smaller semicircle diameters in their impedance spectra and lower interfacial resistance. This indicates that composite separators possess superior induced kinetic performance and can enhance the stability of charge transfer. The body resistances of the PP, PP@3DP, and PP@TOC/3DP separator assembled batteries can be calculated as 3.345, 1.904, and 0.737 Ω, respectively, by the cross-intercept of the curves in Figs. 4(c) and 4(d). Meanwhile, the data show that the ionic conductivities of PP@3DP and PP@TOC/3DP separators are 0.844 and 2.166 mS·cm^{-1}, respectively, both of which are higher than 0.363 mS·cm^{-1} of PP separators (for details, please refer to Table S2 in the ESM). The reason for the enhancement of ion conductivity in composite separator-assembled batteries lies in the regular porous structure of the materials. This architecture not only facilitates the infiltration of greater volumes of electrolyte into the membrane coating, thereby creating abundant reservoirs for electrolyte entrapment, but also expands lithium-ion transport

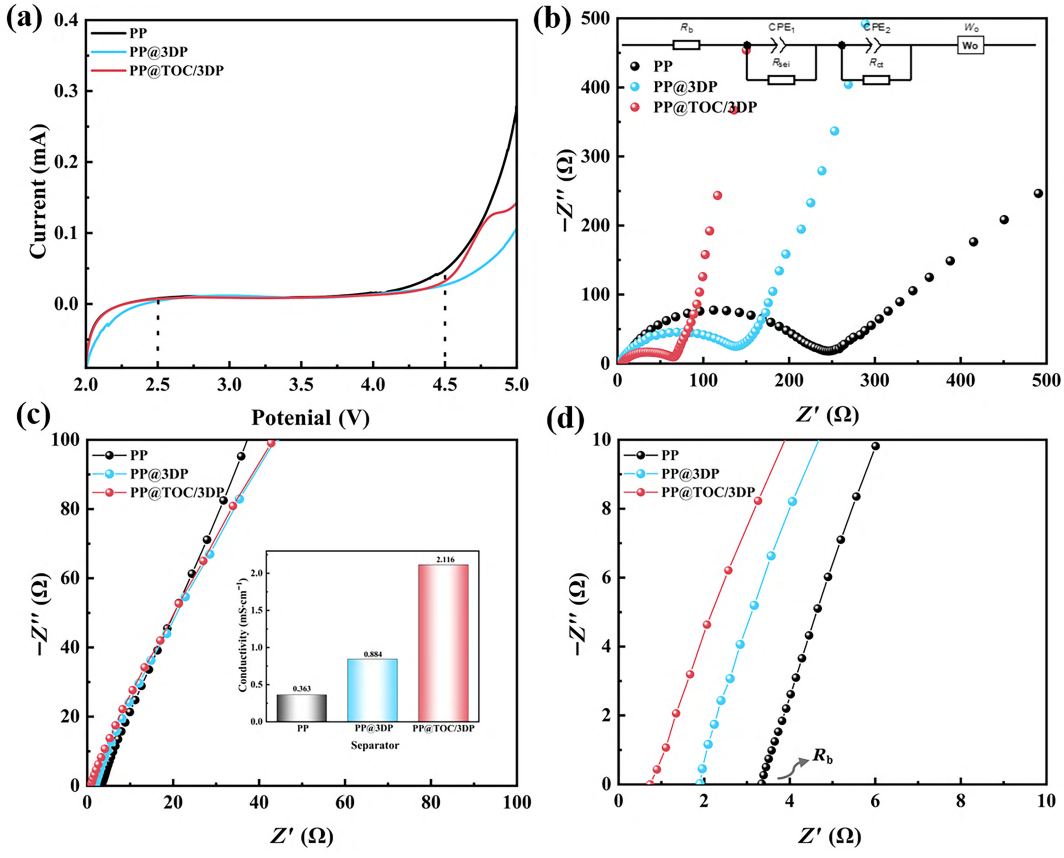

Figure 4 (a) Electrochemical window, (b) Nyquist curves of LFP//Li assembled with three separators, (c) ionic conductivity, and (d) enlarged ionic conductivity of PP, PP@3DP, and PP@TOC/3DP separators.

pathways by enhancing porosity—ultimately enabling the rapid and unimpeded translocation of lithium ions across the membrane [38, 39]. In addition, to evaluate the impact of different separators on the ion transport performance of the battery, the current–time (*I*–*t*) curves (large figure) and electrochemical impedance spectroscopy (EIS) curves (small figure) of symmetric batteries assembled with PP, PP@3DP, and PP@TOC/3DP separators are shown in Fig. S10 in the ESM. Detailed numerical values are provided in Table S3 in the ESM. After calculation, the lithium-ion migration numbers of the symmetrical batteries assembled with PP@3DP and PP@TOC/3DP composite separators are 0.62 and 0.76, respectively, which are much higher than the lithium-ion migration number of 0.53 of the PP lithium symmetrical battery. This is attributed to the fact that the composite separator has a good affinity with the electrolyte directly, reducing the impedance of interfacial transmission, as well as the fact that 3DP and TOC/3DP themselves have rich pores and interlayer gaps, which increase the porosity of the separator and the retention rate of the electrolyte, promote the diffusion of ions and electrons, and provide a platform for the uniform redistribution of lithium ions.

CV curves of the LFP//Li battery are recorded at scan rates of 0.1–0.5 mV·s^{-1}. Figures 5(a)–5(c) show these curves, which reveal the presence of peak current (I_p) near 3.3–3.75 V, which is closely related to the electrochemical reactions occurring between lithium ions and LFP. Compared with the batteries equipped with PP separators, the batteries with PP@3DP and PP@TOC/3DP separators exhibit significantly enhanced reaction kinetics. Meanwhile, the linear correlation between the peak current and the square root of the scanning speed is observed, indicating that the diffusion coefficients of lithium ions in the batteries equipped with composite separators exceed those based on PP in Fig. 5(d), which indicates enhanced lithium-ion diffusion kinetics in batteries based on PP@3DP and PP@TOC/3DP.

At a low current rate of 0.1 C, the discharge specific capacities of the lithium metal batteries assembled with PP@3DP and PP@TOC/3DP composite separators are 159.85 and 169.93 mAh·g^{-1}, respectively, both of which are higher than that of the battery assembled with the PP separator, which is 145.98 mAh·g^{-1}; the detailed values are shown in Table S4 in the ESM. As the current density of battery charging and discharging increases, the requirement for the lithium-ion transport capacity of the battery also rises. The ion conductivity and lithium-ion transference number of batteries assembled with PP@3DP and PP@TOC/3DP separators are both higher than those of batteries assembled with PP separators, which can meet the demand for battery cycling at high current densities. After cycling five times at different current densities ranging from 0.1 to 2 C, when the rate returns to 0.1 C, the PP@3DP and PP@TOC/3DP batteries still maintain relatively high specific capacities of 157.05 and 170.03 mAh·g^{-1} in Fig. 6(a), respectively, indicating that the batteries assembled with PP@3DP and PP@TOC/3DP separators have better cycling reversibility than those assembled with PP separators.

In the cycle test with a factor of 0.5 C, the initial discharge capacities of the batteries assembled with PP@3DP and PP@TOC/3DP separators are 148.91 and 167.96 mAh·g^{-1}, respectively, while that of the battery with a PP separator is 139.29 mAh·g^{-1}. After about 100 cycles, all batteries show a capacity decline trend. Particularly, the battery with a PP separator begins to

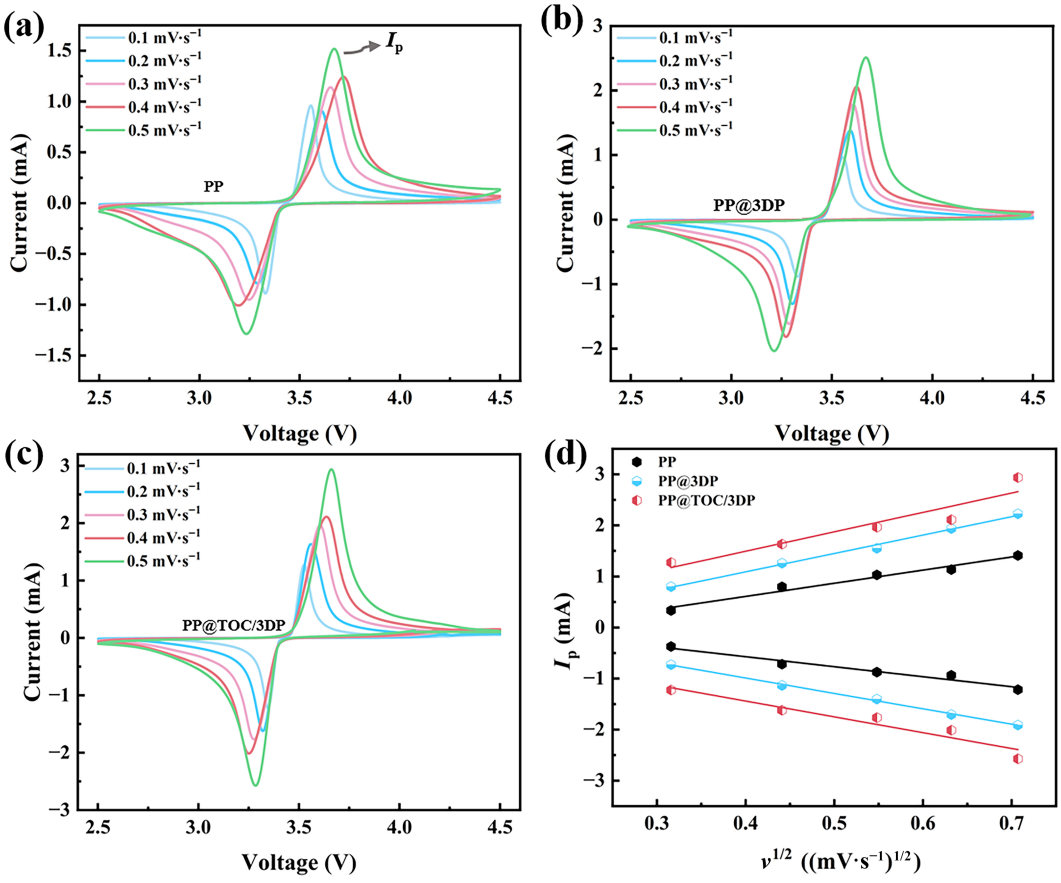

Figure 5 (a) PP, (b) PP@3DP, and (c) PP@TOC/3DP CV curves at scan rates of 0.1–0.5 mV·s^{-1}. (d) Linear relationship between I_p and square root of scan rate ($v^{1/2}$).

decline after 50 cycles, while the battery with a PP@3DP separator has a slightly milder decline. The battery with a PP@TOC/3DP separator demonstrates the best cycling stability among all and can still stably charge and discharge. By the 300th cycle, the capacity retention rates of the batteries assembled with PP, PP@3DP, and PP@TOC/3DP separators are 81.43%, 86.36%, and 97.23% in Fig. 6(b), respectively. The main reason is that the porous structure and compositional components of 3DP and TOC/3DP, when used as coatings, can enhance the physical properties of the separator, effectively suppress the growth and penetration of lithium dendrites through the separator, and improve the battery capacity [40]. Furthermore, Fig. 6(c) more intuitively demonstrates the excellent cycle stability of the PP@TOC/3DP battery. The battery assembled with the PP separator exhibits a significantly larger difference in specific capacity after 1 to 300 cycles at 0.5 C, whereas the specific capacity of the PP@3DP battery decreases more gradually, and the specific capacity of the PP@TOC/3DP battery decreases even more slowly. The results show that 3DP and TOC/3DP coatings can significantly optimize the performance of PP separators: These coatings not only effectively shorten the diffusion path of lithium ions, accelerate the transmission rate of lithium ions, and promote the uniform distribution of lithium ions on the electrode surface [41]. Additionally, they can effectively enhance the thermal stability and mechanical strength of the separators, providing more reliable structural support for their practical applications, thereby improving battery safety and durability.

In the cycle test with a factor of 1.0 C, the capacity of the battery equipped with a PP separator has been continuously decreasing, while the capacity of the battery equipped with a composite separator fluctuates little in the first 600 cycles and then shows a slight downward trend. The initial discharge capacities of the batteries assembled with PP@3DP and PP@TOC/3DP are 138.10 and 160.89 mAh·g^{-1}, respectively, and the initial discharge capacity of the battery with the PP separator is 114.9 mAh·g^{-1}. After 650 cycles, the battery assembled with the PP separator suffers an abrupt short-circuit failure, and its voltage drops instantaneously to 0 V. As a result, this battery is unable to continue the charge–discharge cycle efficiency evaluation. In Fig. 6(d), the capacity retention rates of the batteries with PP@3DP and PP@TOC/3DP separators after 800 cycles are 78.67% and 94.92%, respectively. It is obvious that the capacity holding rate of batteries assembled with composite separators is higher than that of batteries assembled with PP, and the Coulombic efficiency of batteries using composite separators is more stable, demonstrating superior electrochemical performance, among which the performance of batteries assembled with PP@TOC/3DP separators is particularly remarkable.

The cycling performance test of lithium metal batteries assembled with three types of separators is conducted at a current density of 2.0 C. Compared with the PP separator, the LFP//Li half-battery assembled with the PP@TOC/3DP separator exhibits higher discharge specific capacity and improved cycle life durability. The initial capacity of the commercial PP separator battery is 107.99 mAh·g^{-1}. After 100 cycles at 2.0 C, the specific capacity begins to decrease significantly. This is because lithium dendrites grow rapidly under high current density, leading to irreversible loss of lithium ions, which in turn causes a decline in discharge specific capacity. The PP@3DP initial capacity of the separator battery is

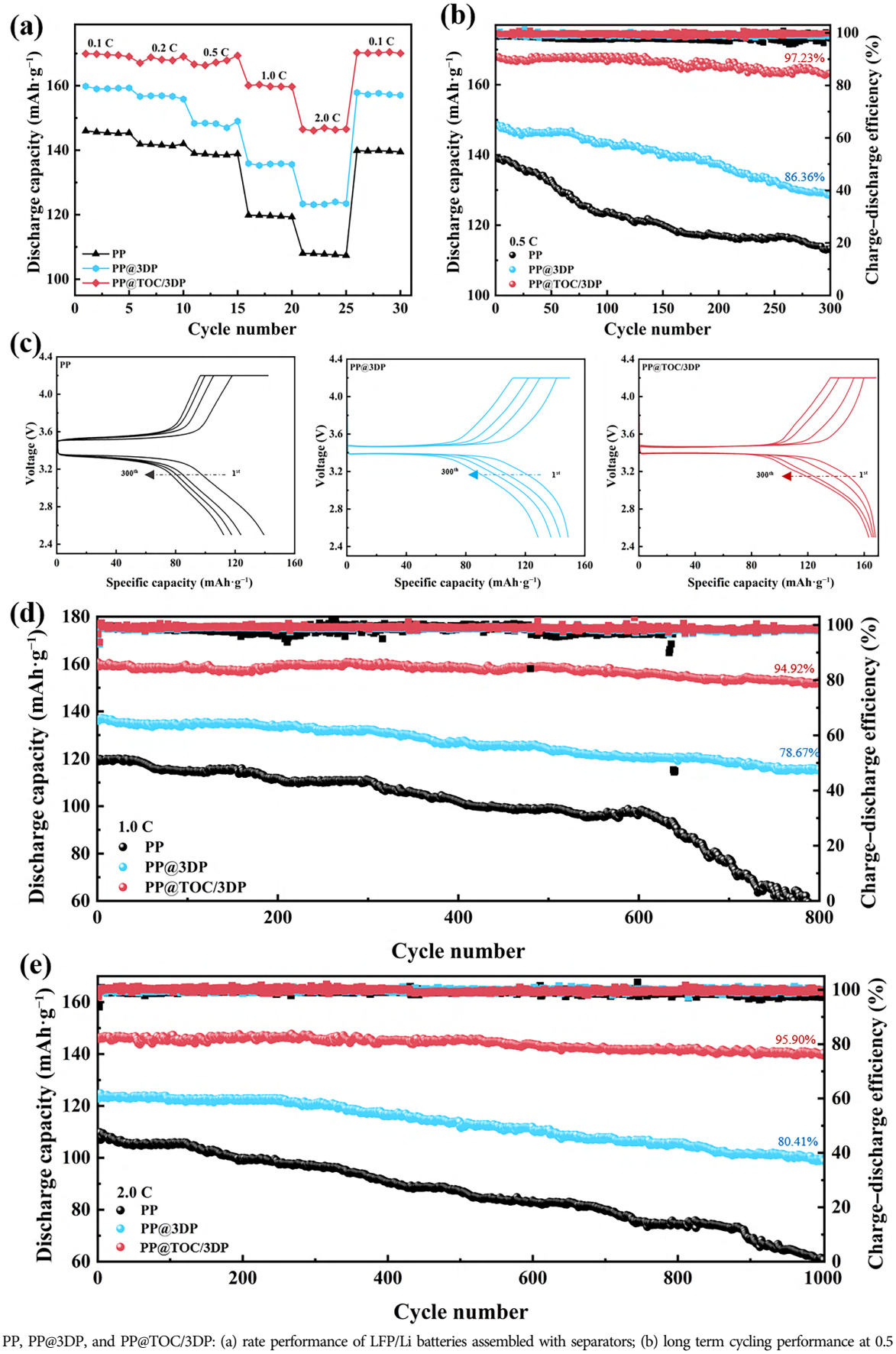

Figure 6 PP, PP@3DP, and PP@TOC/3DP: (a) rate performance of LFP/Li batteries assembled with separators; (b) long term cycling performance at 0.5 C rate; (c) specific capacity–voltage curves of 1–300 cycles at 0.5 C rate; (d) long term cycling performance at 0.1 C rate; and (e) long term cycling performance at 2.0 C rate.

122.91 mAh·g^{-1}. After 1000 cycles, the capacity retention rate is 80.41%. The PP@TOC/3DP separator battery performs the best, with an initial capacity of 146.36 mAh·g^{-1}. After 1000 cycles at 2.0 C, the capacity remained 140.36 mAh·g^{-1}, with a capacity retention rate as high as 95.90%, and the Coulombic efficiency remains stable all the time in Fig. 6(e). Under the action of the template agent, TOC/3DP forms characteristics with a large specific surface area and rich pore structure, which can provide sufficient active sites and efficient channels for lithium ion transport. This characteristic confirms that the PP@TOC/3DP separator has significant value in enhancing the energy density of lithium batteries and improving their cycle stability, providing strong support for the performance optimization of lithium batteries.

To investigate the long-term cyclic durability of composite separators and their inhibitory effect on lithium dendrites, this study assembles Li//Li symmetric batteries using PP, PP@3DP, and PP@TOC/3DP separators, and conducts galvanostatic charge–discharge tests at a current density of 0.1 mA·cm^{-2} (with each complete charge–discharge cycle lasting 1 h). During this process, lithium ions shuttle back and forth between the lithium metal electrode and are repeatedly plated/stripped [42]. The time–voltage curves of lithium symmetric batteries are shown in Figs. 7(a)–7(e), and the corresponding SEM images of the lithium electrode are presented in Fig. 7(f). At the beginning of the test, the battery performance gradually activates and the SEI film forms, and the overpotential of the three types of separator batteries all decreases. After full activation, the overpotential of the PP@3DP and PP@TOC/3DP separator batteries is lower, approximately 0.063 and 0.045 V, respectively, while that of the PP separator battery is approximately 0.075 V in Fig. 7(a). But all three reach a

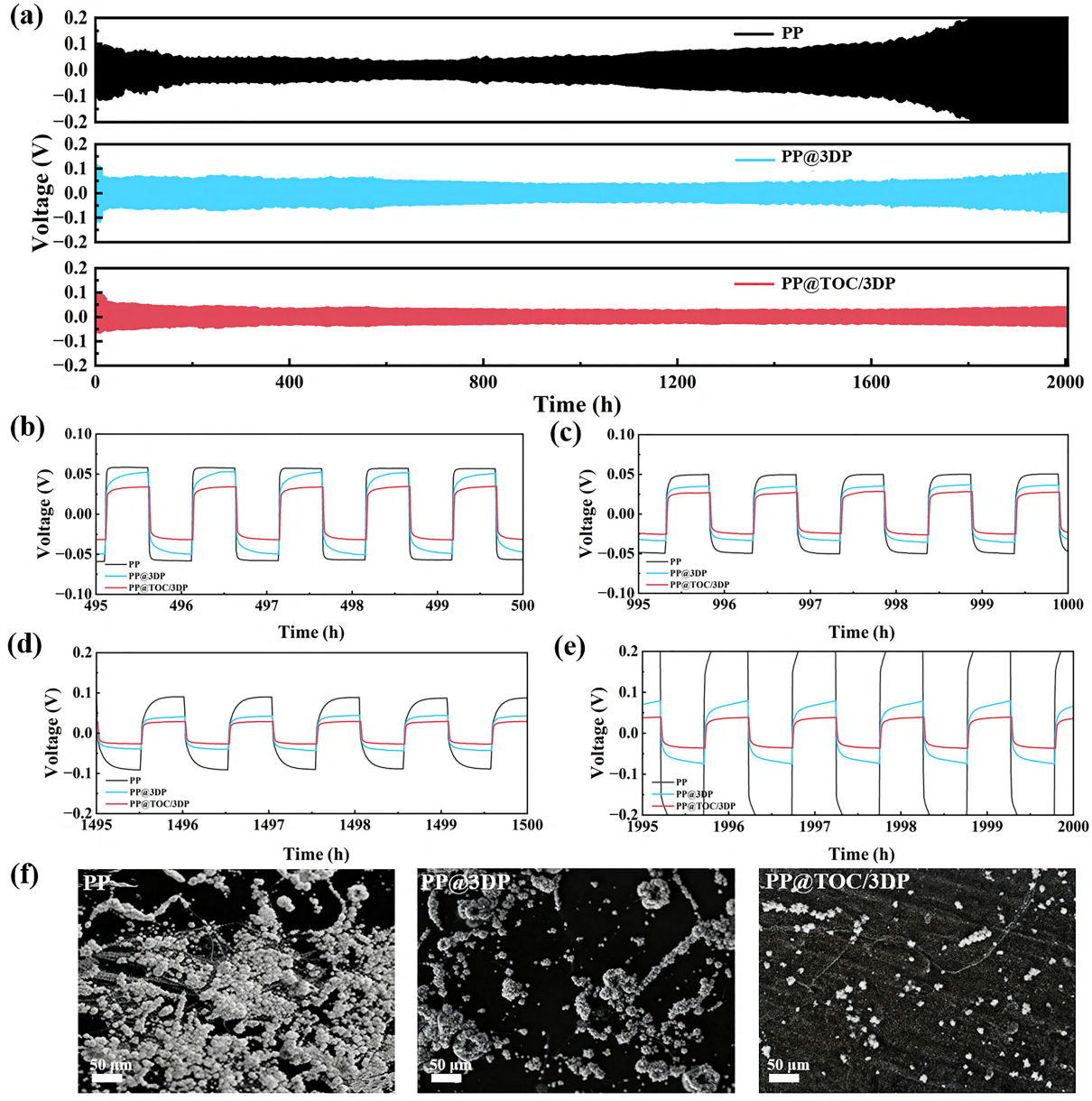

Figure 7 (a) PP, PP@3DP, PP@TOC/3DP. Voltage–time curves and voltage–time amplification of lithium symmetric batteries assembled with separators cycled at a current density of 0.1 mA·cm^{-2}: (b) 495–500 h, (c) 995–1000 h, (d) 1495–1500 h, and (e) 1995–2000 h. (f) Scanning electron microscopy images of the lithium electrode surface of the battery after 500 cycles.

stable state at 495–500 h in Fig. 7(b), the average overpotential of the PP battery (0.057 V) is still greater than that of PP@3DP (0.047 V) and PP@TOC/3DP (0.031 V). After the initial gradual stabilization process of PP@3DP and PP@TOC/3DP separator batteries, the cycle life can reach 2000 h. After an initial gradual stabilization process, the cycle life of PP@3DP and PP@TOC/3DP membrane batteries can reach 2000 h. The PP@3DP battery shows an increased overpotential after 1600 h, while the PP@TOC/3DP battery exhibits only a slight rise in overpotential at 2000 h and maintains a low value. The average overpotentials for the two batteries between 1995 and 2000 h are 0.066 and 0.036 V in Fig. 7(e), respectively. The cycling stability of PP@3DP and PP@TOC/3DP separators is superior, mainly due to the synergistic effect of their performance advantages: The composite separator itself has a higher ionic conductivity, lithium ion migration number, and better mechanical properties; the 3DP and TOC/3DP in the coating bring high stability, abundant polar groups, and good electrolyte affinity [43]. These characteristics jointly improve the interfacial compatibility between the lithium anode and the separator, promoting the uniform distribution and redistribution of lithium ions, thereby alleviating and inhibiting the growth of lithium dendrites, and ultimately ensuring the stability and reversibility of the lithium intercalation/deintercalation and electroplating/stripping processes [44, 45].

The morphological changes on the surface of lithium sheets after cycling are also investigated. The SEM image clearly shows the differences among the three types of lithium symmetrical batteries: After 500 cycles at a current density of 0.1 mA·cm^{-2}, the battery with a PP@TOC/3DP separator has the smoothest lithium sheet surface with almost no dendrite formation, indicating that the SEI layer formed in this battery is more uniform and can promote the uniform diffusion of lithium ions during lithium deposition and dissolution [46, 47]. Batteries equipped with PP@3DP separators can significantly reduce the number of lithium dendrites, but the dendrite distribution is not regular enough, and a small number of dendrites appear on the surface [48]. For batteries equipped with PP separators, the surface of the lithium sheets is completely covered with rough moss-like lithium dendrites [49], and there are also large areas of dendritic regions in Fig. 7(f). The results show that 3DP can achieve a uniform distribution of lithium ions by its own uniform pore structure, thereby slowing down the growth rate of lithium dendrites [50]. Among them, the TOC/3DP coating undergoes morphological transformation. The significant increase in specific surface area can expose more active sites, ultimately endowing the PP@TOC/3DP separator with an excellent ability to guide lithium ions to achieve homogeneous deposition, and it performs best in inhibiting lithium dendrite growth [51]. Furthermore, we conduct a comparative analysis of the main properties of the lamellar molecular sieve coating (PP@TOC/3DP) used as a battery separator with previous research results in Table S5 in the ESM. The results show that the PP@TOC/3DP separator exhibits significantly higher discharge capacity and lower capacity decay rate. These excellent performances are mainly attributed to the large specific surface area and abundant and uniformly distributed pore structure of the lamellar material, which provides a more uniform and efficient transmission platform for lithium ions within the battery. Through the aforementioned multi-faceted performance improvements, the growth of lithium dendrites is ultimately successfully inhibited, effectively preventing the phenomenon of lithium dendrites penetrating the separator, thus ensuring the long-term stable operation and safety of the entire battery system.

4 Conclusions

In conclusion, we have successfully developed two composite separators, namely PP@3DP and PP@TOC/3DP, for LMBs. Due to the inherent rich porous structure, excellent thermal resistance, and hydrophilicity of molecular sieves, the thermal shrinkage rate of the modified separator is notably reduced, the electrolyte affinity is substantially enhanced, and the uniform diffusion of lithium ions is effectively promoted. The results indicate that, in comparison with PP and PP@3DP, the PP@TOC/3DP separator is capable of effectively suppressing the growth of lithium dendrites and minimizing electrolyte loss. The assembled LFP//Li full battery retains a high capacity retention rate of 95.90% after 1000 cycles at 2.0 C. Moreover, the assembled lithium plating/stripping battery exhibits a cycle stability of up to 2000 h at a current density of 0.1 mA·cm^{-2}. This study presents a novel approach to the design of LMB separator materials, providing a reliable and practical pathway for the development of high-performance LMBs.

Electronic Supplementary Material: Supplementary material (including detailed experimental procedures, additional characterization results (such as XRD, infrared, thermogravimetric, scanning electron microscopy, electrochemical testing data), and related discussion content) is available in the online version of this article at https://doi.org/10.26599/NR.2026.94908517.

Data availability

All data needed to support the conclusions in the paper are presented in the manuscript and the Electronic Supplementary Material. Additional data related to this paper may be requested from the corresponding author upon request.

Acknowledgements

This work was supported by the Guizhou Provincial Basic Research Program (Natural Science) (No. Qian Ke He Basic-MS [2025] 579), the Guizhou Province Science and Technology Support Project (No. [2023] 170), Advanced Electrochemical Energy Storage Devices and Key Materials Technology Innovation Talent Team Construction of Guizhou Province (No. QKEPTRC-CXTD [2023] 016) and Basic Research Project of Guizhou University (No. [2024] 2). The authors would like to thank Scientific Compass (www.shiyanjia.com) for the XRD characterization and eceshi (www.eceshi.com) for the BET characterization.

Declaration of competing interest

All the contributing authors report no conflict of interests in this work.

Author contribution statement

Q. S.: Writing – review & editing. F. S.: Writing – original draft, methodology. Y. Y. D.: Investigation, formal analysis. S. Y. W.: Data curation, formal analysis. P. W.: Writing – review &editing, supervision, conceptualization. J. Y. H.: Formal analysis. K. N. S.: Formal analysis. J.-J. S.: Writing – review & editing, funding acquisition. All the authors have approved the final manuscript.

Use of AI statement

None.

References

[1] Huang, B. D.; Cai, Z. W.; Tan, Y. X.; Zhang, N.; Peng, T.; Liu, W.; Zhong, H.; Mai, Y. H. Extending the low-temperature operation of lithium-metal batteries combining $LiNO_3$-based eutectic additive and 3D lithium-metal anode. *ACS Sustain. Chem. Eng.* **2024**, *12*, 8276–8285.

[2] Dubaniewicz, T. H.; DuCarme, J. P. Are lithium ion cells intrinsically safe. *IEEE Trans. Ind. Appl.* **2013**, *49*, 2451–2460.

[3] Lin, M. Y.; Chen, Y. Q.; Wang, C. Y.; Xu, S. M.; Zhang, J. L. Towards preferential lithium recovery from spent lithium-ion batteries: Phase transition mechanisms, technical innovation and future perspectives. *Prog. Mater. Sci.* **2026**, *156*, 101557.

[4] Sauer, N. G.; Gaudet, B.; Barowy, A. Experimental investigation of explosion hazard from lithium-ion battery thermal runaway effluent gas. *Fuel* **2024**, *378*, 132818.

[5] Parvizi, P.; Jalilian, M.; Amidi, A. M.; Zangeneh, M. R.; Riba, J. R. From present innovations to future potential: The promising journey of lithium-ion batteries. *Micromachines* **2025**, *16*, 194.

[6] Jang, J.; Oh, J.; Jeong, H.; Kang, W.; Jo, C. A review of functional separators for lithium metal battery applications. *Materials* **2020**, *13*, 4625.

[7] Yeh, W. T.; Huang, Y. F.; Wu, C. C.; Hong, P. D. Structure and morphological changes of multilayer separators for lithium-ion batteries under abuse/overcharge conditions. *J. Appl. Polym. Sci.* **2022**, *139*, 52046.

[8] Heidari, A. A.; Mahdavi, H. Recent development of polyolefin-based microporous separators for Li-ion batteries: A review. *Chem. Rec.* **2020**, *20*, 570–595.

[9] Singh, A. K.; Yadav, R.; Rosy. Zinc oxide nanoplatelet-coated polypropylene separators as a bifunctional tool for enabling dendrite-free lithium metal batteries: A binder-free approach. *ACS Appl. Mater. Interfaces* **2025**, *17*, 40409–40421.

[10] Liu, H.; Jin, B.; Gao, N.; Jiang, Q. Multishelled hollow spherical high entropy oxide as a separator modification layer toward stable lithium-metal batteries. *Nano Lett.* **2025**, *25*, 11768–11775.

[11] Hijazi, N.; Bavykina, A.; Yarulina, I.; Shoinkhorova, T.; Ramos-Fernandez, E. V.; Gascon, J. Chemical engineering of zeolites: Alleviating transport limitations through hierarchical design and shaping. *Chem. Soc. Rev.* **2025**, *54*, 6335–6384.

[12] Cho, J.; Ishida, Y. Macroscopically oriented porous materials with periodic ordered structures: From zeolites and metal–organic frameworks to liquid-crystal-templated mesoporous materials. *Adv. Mater.* **2017**, *29*, 1605974.

[13] Yu, Y.; Yang, F.; Chen, X. L.; Lu, M. X.; Zou, J.; Xu, F.; Huang, K.; Xu, Z. MFI zeolite nanosheet composite membranes with both high lithium ion transport and sulfur fixation for lithium–sulfur batteries. *Ind. Eng. Chem. Res.* **2025**, *64*, 8425–8432.

[14] Wang, S. Y.; Wang, P.; Deng, Y. Y.; Sha, F.; Zhao, P.; Cao, J.; Shen, J.; Sun, Q.; Shao, J. J.; Wang, Y. Y. Efficient mitigation of lithium dendrite by two-dimensional A-type molecular sieve membrane for lithium metal battery. *J. Colloid Interface Sci.* **2025**, *678*, 251–259.

[15] Sharma, P.; Song, J. S.; Han, M. H.; Cho, C. H. GIS-NaP1 zeolite microspheres as potential water adsorption material: Influence of initial silica concentration on adsorptive and physical/topological properties. *Sci. Rep.* **2016**, *6*, 22734.

[16] Bhaumik, A.; Inagaki, S. Mesoporous titanium phosphate molecular sieves with ion-exchange capacity. *J. Am. Chem. Soc.* **2001**, *123*, 691–696.

[17] Strohmaier, K. G.; Vaughan, D. E. W. Structure of the first silicate molecular sieve with 18-ring pore openings, ECR-34. *J. Am. Chem. Soc.* **2003**, *125*, 16035–16039.

[18] Buttersack, C. Modeling of type IV and V sigmoidal adsorption isotherms. *Phys. Chem. Chem. Phys.* **2019**, *21*, 5614–5626.

[19] Zhang, L. D.; Jee, S.; Park, J.; Jung, M.; Wallacher, D.; Franz, A.; Lee, W.; Yoon, M.; Choi, K.; Hirscher, M. et al. Exploiting dynamic opening of apertures in a partially fluorinated MOF for enhancing H_2 desorption temperature and isotope separation. *J. Am. Chem. Soc.* **2019**, *141*, 19850–19858.

[20] Tsotsalas, M.; Hejcik, P.; Sumida, K.; Kalay, Z.; Furukawa, S.; Kitagawa, S. Impact of molecular clustering inside nanopores on desorption processes. *J. Am. Chem. Soc.* **2013**, *135*, 4608–4611.

[21] Baerlocher, C. H.; Meier, W. M. The crystal structure of synthetic zeolite Na–P1, an isotype of gismondine. *Z. Kristallogr. Cryst. Mater.* **1972**, *135*, 339–354.

[22] Cychosz, K. A.; Guillet-Nicolas, R.; García-Martínez, J.; Thommes, M. Recent advances in the textural characterization of hierarchically structured nanoporous materials. *Chem. Soc. Rev.* **2017**, *46*, 389–414.

[23] Chudasama, C. D.; Sebastian, J.; Jasra, R. V. Pore-size engineering of zeolite A for the size/shape selective molecular separation. *Ind. Eng. Chem. Res.* **2005**, *44*, 1780–1786.

[24] Segal, E.; Maistriau, L.; Derouane, E. G.; Gabelica, Z. TG and DSC investigation of the dehydration of the extra large pore aluminophosphate molecular sieve VPI-5 and related materials. *J. Therm. Anal.* **1994**, *41*, 701–712.

[25] Shelyapina, M. G.; Yocupicio-Gaxiola, R. I.; Zhelezniak, I. V.; Chislov, M. V.; Antúnez-García, J.; Murrieta-Rico, F. N.; Galván, D. H.; Petranovskii, V.; Fuentes-Moyado, S. Local structures of two-dimensional zeolites-mordenite and ZSM-5-probed by multinuclear NMR. *Molecules* **2020**, *25*, 4678.

[26] Shelyapina, M. G.; Krylova, E. A.; Mazur, A. S.; Tsyganenko, A. A.; Shergin, Y. V.; Satikova, E. A.; Petranovskii, V. Active sites in H-mordenite catalysts probed by NMR and FTIR. *Catalysts* **2023**, *13*, 344.

[27] Kannan, D. R. R.; Terala, P. K.; Moss, P. L.; Weatherspoon, M. H. Analysis of the separator thickness and porosity on the performance of lithium-ion batteries. *Int. J. Electrochem.* **2018**, *2018*, 1925708.

[28] Din, M. M. U.; Murugan, R. Metal coated polypropylene separator with enhanced surface wettability for high capacity lithium metal batteries. *Sci. Rep.* **2019**, *9*, 16795.

[29] Neupane, S.; Chiriaev, S.; Greenbank, W.; Gkionis-Konstantatos, O.; Leissner, T.; Ebel, T.; Tavares, L. Nanoscale thinning of metal-coated polypropylene films by Helium-ion irradiation. *Power Electron. Devices Compon.* **2023**, *6*, 100046.

[30] Li, Y. J.; Sha, L. T.; Lv, P. L.; Qiu, N.; Zhao, W.; Chen, B.; Hu, P.; Zhang, G. Influences of separator thickness and surface coating on lithium dendrite growth: A phase-field study. *Materials* **2022**, *15*, 7912.

[31] Ren, W. X.; Zhu, K. R.; Zhang, W.; Liang, H. C.; Xu, L.; Wang, L. P.; Yang, C. C.; Yang, Y.; Zhang, P. F.; Wang, F. et al. Dendrite-free lithium metal battery enabled by dendritic mesoporous silica coated separator. *Adv. Funct. Mater.* **2023**, *33*, 2301586.

[32] Liu, Q. Z.; Xia, M.; Chen, J. H.; Tao, Y. F.; Wang, Y. D.; Liu, K.; Li, M. F.; Wang, W. W.; Wang, D. High performance hybrid Al_2O_3/poly (vinyl alcohol-ethylene) nanofibrous membrane for lithium-ion battery separator. *Electrochim. Acta* **2015**, *176*, 949–955.

[33] Yu, L. H.; Miao, J. S.; Jin, Y.; Lin, J. Y. S. A comparative study on polypropylene separators coated with different inorganic materials for lithium-ion batteries. *Front. Chem. Sci. Eng.* **2017**, *11*, 346–352.

[34] Moghim, M. H.; Nahvi Bayani, A.; Eqra, R. Strain-rate-dependent mechanical properties of polypropylene separator for lithium-ion batteries. *Polym. Int.* **2020**, *69*, 545–551.

[35] An, H.; Roh, Y.; Jo, Y.; Lee, H.; Lim, M.; Lee, M.; Lee, Y. M.; Lee, H. Separator dependency on cycling stability of lithium metal batteries under practical conditions. *Energy Environ. Mater.* **2023**, *6*, e12397.

[36] Fan, Z. X.; Chen, X. Y.; Shi, J. J.; Nie, H.; Zhang, X. M.; Zhou, X. P.; Xie, X. L.; Xue, Z. G. Functionalized separators boosting

electrochemical performances for lithium batteries. *Nano-Micro Lett.* **2025**, *17*, 128.
[37] Kim, P. J. Surface-functionalized separator for stable and reliable lithium metal batteries: A review. *Nanomaterials* **2021**, *11*, 2275.
[38] Zeng, Q.; Wang, L.; Ma, C. C.; Mai, W. J.; Li, J. L.; Liu, M. X. Halloysite clay nanotube-coated polypropylene separator for dendrite-free and long-life sodium metal batteries. *Energy Storage Mater.* **2025**, *80*, 104372.
[39] Centrella, B.; Deplano, G.; Damin, A.; Signorile, M.; Tortora, M.; Barolo, C.; Bonomo, M.; Bordiga, S. A multi-technique approach to unveil the redox behaviour and potentiality of homoleptic Cu^{I} complexes based on substituted bipyridine ligands in oxygenation reactions. *Dalton Trans.* **2022**, *51*, 14439–14451.
[40] Dong, X. L.; Mi, W. L.; Yu, L. H.; Jin, Y.; Lin, Y. S. Zeolite coated polypropylene separators with tunable surface properties for lithium-ion batteries. *Microporous Mesoporous Mater.* **2016**, *226*, 406–414.
[41] Zhang, G. Z.; Li, J. W.; Chi, S. S.; Wang, J.; Wang, Q. R.; Ke, R. H.; Liu, Z. B.; Wang, H.; Wang, C. Y.; Chang, J. et al. Molecular design of competitive solvation electrolytes for practical high-energy and long-cycling lithium-metal batteries. *Adv. Funct. Mater.* **2024**, *34*, 2312413.
[42] Xie, H. Y.; Hao, Z. M.; Xie, S.; Ye, Y. D.; Zhang, W.; Sun, Z. W.; Jin, S.; Ji, H. X.; Chen, J. Molecular sieve based Janus separators for Li-ions redistribution to enable stable lithium deposition. *Nano Res.* **2022**, *15*, 5143–5152.
[43] Zhao, L. N.; Wu, Z. Y.; Wang, Z. H.; Bai, Z.; Sun, W.; Sun, K. N. Regulating solvation structures enabled by the mesoporous material MCM-41 for rechargeable lithium metal batteries. *ACS Nano* **2022**, *16*, 20891–20901.
[44] Lee, J.; Park, Y.; Choi, J. W. Navigating interfacial challenges in lithium metal batteries: From fundamental understanding to practical realization. *Nano Converg.* **2025**, *12*, 25.
[45] Zhang, Z.; Gou, J. R.; Cui, K. X.; Zhang, X.; Yao, Y. J.; Wang, S. Q.; Wang, H. H. 12.6 μm-thick asymmetric composite electrolyte with superior interfacial stability for solid-state lithium-metal batteries. *Nano-Micro Lett.* **2024**, *16*, 181.
[46] Verma, P.; Puravankara, S.; Nandanwar, M. N.; Chakraborty, J. Insights into the morphological evolution of mossy dendrites in lithium metal symmetric and full cell: A modelling study. *J. Electrochem. Soc.* **2023**, *170*, 030529.
[47] Li, W. Y.; Yao, H. B.; Yan, K.; Zheng, G. Y.; Liang, Z.; Chiang, Y. M.; Cui, Y. The synergetic effect of lithium polysulfide and lithium nitrate to prevent lithium dendrite growth. *Nat. Commun.* **2015**, *6*, 7436.
[48] Jin, D. Q.; Hu, K.; Hou, R.; Shang, H.; Wang, X. Y.; Ding, Y.; Yan, Y.; Lin, H. J.; Rui, K.; Zhu, J. X. Vertical nanoarrays with lithiophilic sites suppress the growth of lithium dendrites for ultrastable lithium metal batteries. *Chem. Eng. J.* **2021**, *405*, 126808.
[49] Jana, A.; Woo, S. I.; Vikrant, K. S. N.; Garcia, R. E. Electrochemomechanics of lithium dendrite growth. *Energy Environ. Sci.* **2019**, *12*, 3099–3114.
[50] McConohy, G.; Xu, X.; Cui, T.; Barks, E.; Wang, S.; Kaeli, E.; Melamed, C.; Gu, X. W.; Chueh, W. C. Applied stress can control lithium intrusions in solid electrolytes. *Nat. Energy* **2023**, *8*, 228–229.
[51] Cao, T. C.; Xu, R.; Cheng, X. P.; Wang, M. M.; Sun, T.; Lu, J. X.; Liu, X. Q.; Zhang, Y. F.; Zhang, Z. Chemomechanical origins of the dynamic evolution of isolated Li filaments in inorganic solid-state electrolytes. *Nano Lett.* **2024**, *24*, 1843–1850.